Journal of Naval Architecture and Marine Engineering
July, 2026
https://doi.org/10.3329/jname.v23i2.78082 https://www.banglajol.info

# INFLUENCE OF SHAPE FACTOR ON A HYBRID NANOFLUID FLOW OVER A PERMEABLE FLAT PLATE WITH NON-FOURIER HEAT FLUX MODEL: AN ANALYSIS OF ENTROPY GENERATION

**G. Kathyayani[1], S. S. Nagendra Rao[1,2]**

[1]Department of Applied Mathematics, Yogi Vemana University, Kadapa – 516005, Andhra Pradesh, India.
kathyagk@yogivemanauniversity.ac.in

[2]Department of Humanities & Sciences, St. Peter's Engineering College, Hyderabad-500100, Telangana, India.
nagendra.satuluri@gmail.com

## Abstract:

*The current study explores the complex dynamics of hybrid nanofluid ($H_2O$+MWCNT+CuO) flow on a flat plate, examining the effects of various physical parameters such as velocity slip, shape factor and thermal radiation. The primary equations of the current problem have been converted into a set of ordinary differential equations through the application of suitable similarity transformations. Subsequently, the bvp4c solver is employed to address them. The three cases involving the shape factor—platelet, cylinder, and spherical—are addressed with the results. The friction factor increases at rates of 0.02383, 0.023825, and 0.023809 for platelet, cylinder, and spherical forms, respectively, as the volume % of multiwalled carbon nanotubes varies from 0 to 0.105. Research indicates that when the Eckert number varies from 0 to 0.6, the heat transmission rate decreases by 0.4444371 for platelet form, 0.444998 for cylindrical form, and 0.444502 for spherical form. Increasing the chemical reaction parameter enhances the mass transfer rate by intensifying the concentration gradient at the surface. When the values of the chemical reaction range from 0 to 0.6, the Sherwood number surges at rates of 0.2827136, 0.2827211, and 0.2827408 for platelet, cylinder and spherical forms respectively.*

***Keywords:*** Magnetic field, entropy generation, velocity slip, thermal radiation

## NOMENCLATURE

| | |
|---|---|
| $\sigma$ | Electrical conductivity [$Sm^{-1}$] |
| *Eck* | Eckert number |
| *St* | Schmidt number |
| $\nu$ | Kinematic viscosity [$m^2 s^{-1}$] |
| $k$ | Thermal conductivity [$Wm^{-1} K^{-1}$] |
| $\Gamma$ | Thermal relaxation parameter |
| $k^*$ | Mean absorption coefficient [$m^2 Kg^{-1}$] |
| *Dm* | Molecular diffusivity [$m^2 s^{-1}$] |
| $\rho$ | Density [$Kgm^{-3}$] |
| $\tau_w$ | Wall shear stress [$Nm^{-2}$] |
| $s_w$ | Wall mass flux [$Kgm^{-2} s^{-1}$] |
| *Mg* | Magnetic field parameter |

***Greek symbols***

| | |
|---|---|
| *Cr* | Dimensionless chemical reaction parameter |
| *Br* | Brinkman number |
| $L_0$ | Velocity slip parameter [$m\ s^{-1}$] |
| $\sigma^*$ | Stefan-Boltzmann constant [$Wm^{-2} K^{-4}$] |
| $L$ | Velocity slip parameter (dimensionless) |
| $K$ | Permeability parameter [$m^2$] |
| $\lambda$ | Porosity parameter |
| $k_1$ | Chemical reaction parameter [$molL^{-2} s^{-1}$] |
| $\delta$ | Mixed convection parameter |
| $\Gamma^*$ | Thermal relaxation time of heat flux |
| *Bi* | Biot number |

## 1. Introduction

Thermal radiation significantly influences fluid flow by altering the energy distribution within the fluid. The interaction of thermal radiation with the fluid involves absorption, emission, and scattering processes, which modify the temperature distribution within the flow domain. These thermal variations subsequently influence the velocity field and pressure distribution of the fluid. The phenomenon becomes more pronounced in high-temperature regimes, with radiative heat exchange dominating the transport process. Applications of this

  Received on: Nov. 2024

knowledge include optimizing cooling systems in power plants and aerospace vehicles, designing efficient solar thermal collectors, and understanding the dynamics of astrophysical plasmas. In 1996, Bakier and Reddy explored the effect of thermal radiation on mixed convection over a permeable boundary. Later, Mohammadein and colleagues (2000) applied a comparable configuration to power-law fluids, highlighting how radiative transfer influences their flow properties. When the radiation parameter is amplified, a steeper velocity profile can be seen. Al-Harbi (2005) quantitatively investigated the non-Darcy and radiative movement of a liquid with variable viscosity. The inclusion of a viscosity parameter has been shown to enhance the Nusselt number. The impact of radiation on viscous fluid flow over an exponentially stretching surface was studied by Bidin and Nazar (2009). Makinde et al. (2017) extended this line of inquiry to Walter-B fluid in a flexible conduit, showing that the friction coefficient grows with the Hartmann number. Reddy et al. (2018) further examined radiative Casson nanofluid flow over a cylinder under slip boundary conditions using numerical methods. Findings indicate that higher Eckert numbers suppress fluid velocity, highlighting the role of viscous dissipation. Building on this, Hassan and Fenuga (2019) analyzed the steady radiative flow of a couple-stress fluid through a permeable channel. Results confirmed that entropy generation is most intense along the central axis of the channel. Building on this, Lund et al. (2020) employed the shooting method to study stagnation-point flow in radiative Casson fluids interacting with contracting and expanding surfaces. Further contributions came from Anantha et al. (2020), who analyzed the heat transfer behavior of unsteady Casson fluids over exponentially stretching curved surfaces, with particular attention to viscous dissipation effects. Qasem et al. (2021) later employed the finite difference method to numerically study how thermal radiation affects natural convection and heat transfer in a water-based nanofluid confined within a heated enclosure. Revathi et al. (2021) examined the dissipative and radiative behavior of a hybrid nanofluid flowing over a curved, stretching sheet. Their analysis revealed that higher activation energy parameters are associated with increased concentration levels. Following these studies, several researchers examined the role of thermal radiation across diverse fluid-flow configurations. Notable contributions include the works of Kathyayani (2021), Babu et al. (2022), Appidi et al. (2022), Nadeem et al. (2023), Waqas et al. (2023), Revathi et al. (2024), and Shaheen et al. (2024).

Recent advances in thermal engineering highlight the importance of nanofluids and hybrid nanofluids, primarily due to their remarkable heat transfer capabilities. These engineered fluids are produced by suspending nanoparticles within a conventional base liquid, a modification that significantly enhances thermal conductivity and improves the efficiency of heat transport processes. By incorporating two or more distinct nanoparticle materials into the same base fluid, hybrid nanofluids provide even greater improvements in thermal efficiency than single-particle nanofluids. These advanced fluids find applications in various fields, including electronics cooling, solar energy systems, automotive engines, and biomedical engineering. By improving heat transfer efficiency, they contribute to energy conservation, reduced system size, and enhanced performance in diverse technological applications. According to the research of Koo and Kleinstreuer (2005), the benefits of incorporating nanoparticles can be amplified by using a conventional fluid with a high Prandtl number, such as ethylene glycol. Entropy generation in nanofluid systems was investigated by Moghaddami et al. (2011), who considered flow through a circular tube exposed to constant wall heat flux. Their findings emphasized that nanoparticle dispersion can improve thermodynamic efficiency provided that heat transfer irreversibility remains the leading source of entropy generation. Building on this foundation, Thameem Basha et al. (2019) explored stagnation-point flow and the heat transfer characteristics of nanofluids formulated with ethylene glycol and water. The microscale dynamics of CNT–water nanofluids over irregular radially stretching disks were analyzed by Gohar et al. (2019) using the homotopy analysis method. Extending this line of inquiry, Upreti and Kumar (2020) investigated how Ohmic heating and thermal radiation jointly influence nanofluid flow across slender needles, reporting that water-based fluids achieved the highest velocities, whereas ethylene glycol yielded the lowest. More recently, Majeed et al. (2023) and Makhdoum et al. (2023) contributed further insights by modeling flow and heat transfer characteristics of nanofluids over stretching surfaces through varied mathematical formulations. Hussain et al. (2017) expended the FEM to examine the optimization of entropy generation for the water + $Al_2O_3$ +Cu fluid flow within a horizontal conduit. Findings indicated that heat transfer intensifies as the Richardson number increases. Extending this line of research, Afridi et al. (2018) analyzed the dissipative flow dynamics of the same fluid over an exponentially stretching sheet, offering further insight into its thermal behavior. It has been found that in hybrid nanofluids, fluid friction irreversibility is more pronounced than in convectional nanofluids. In 2020, Acharya and colleagues applied the RK-4 scheme to study radiative flow of a water + $TiO_2$ + $CoFe_2O_4$ particles over a spinning disc. It has been found that compared to a single particle, the thermal efficiency of a suspension of two particles is greatly enhanced. In their study of flow characteristics in a micropolar (water + $Al_2O_3$ + Cu) hybrid nanofluid, Roy et al. (2021) used a contracting/expanding surface with a vortex viscosity parameter to produce two solutions. Results show that as the vortex viscosity parameter is decreased, so does the temperature profile. Research momentum continued with contributions from Sandeep et al. (2022), Animasaun et al. (2022), Cao et al. (2022), Xiu et al. (2022), Ullah et al. (2023), and Ali et al. (2024), who collectively investigated how hybrid nanofluids behave in terms of heat and mass transfer when subjected to a wide range of geometrical configurations.

The central contribution of this research lies in its detailed examination of flow and heat transfer in a Water–MWCNT–CuO hybrid nanofluid. By accounting for the combined impacts of thermal radiation, higher-order chemical reactions, and the Cattaneo–Christov heat flux framework, the study provides new insights into the complex mechanisms governing hybrid nanofluid performance. Although these physical mechanisms have been examined separately in earlier studies, their combined influence, particularly in the presence of varying nanoparticle shape factors, has not been systematically explored. We present the outcomes for the various shape factor scenarios: spherical, platelet and cylindrical. The relevant physical features are shown and explained using tables and bar graphs. This investigation set out to address a number of interrelated questions:

1. Nanoparticle Geometry and Radiation
Among platelet, cylindrical, and spherical nanoparticle geometries, which configuration exerts the greatest impact on fluid flow behavior when exposed to thermal radiation?
2. Thermal Relaxation and Convective Heating
In systems governed by convective boundary conditions, what role does the thermal relaxation parameter play in shaping the fluid's temperature distribution?
3. Magnetic Field and Slip Flow
Under slip boundary conditions, how does variation in the magnetic field parameter alter the velocity and transport characteristics of hybrid nanofluids?
4. What changes take place in the formation of entropy profile as the volume proportion of MWCNT?

## 2. Mathematical formulations

This study focuses on analyzing the flow characteristics of an aqueous hybrid nanofluid past a flat plate. The governing mathematical framework is formulated under a set of defined assumptions.

(i) For the computational analysis, the thermo-physical properties of MWCNT, CuO, and water were utilized as provided in Table 1.

(ii) The schematic representation in Figure 1 shows the flow arrangement, where a uniform magnetic field of strength $B$ is applied perpendicular to the flat plate, thereby influencing the fluid motion.

(iii) At the plate surface, the fluid satisfies the no-slip condition, adhering completely to the boundary and yielding zero velocity. Progressively away from the wall, the velocity increases and asymptotically approaches the free-stream value $U_\infty$ beyond the boundary-layer region.

(iv) In the present model, the magnetic field induced by the motion of the conducting fluid is assumed negligible and hence excluded. With these simplifications, the governing conservation equations together with the associated boundary conditions are formulated (Purna Chandar Rao et al., 2022; Makinde, 2013; Al-Hossainy and Eid, 2021).

$$\frac{\partial v}{\partial y}+\frac{\partial u}{\partial x}=0 \tag{1}$$

$$v\frac{\partial u}{\partial y}+u\frac{\partial u}{\partial x}=\frac{1}{\rho_{hnf}}\mu_{hnf}\frac{\partial^2 u}{\partial y^2}+\beta_T g(T-T_\infty)-(u-U_\infty)\frac{\sigma_{hnf}}{\rho_{hnf}}B^2$$
$$-\frac{1}{\rho_{hnf}}\frac{\mu_{hnf}}{\kappa}u+\beta_C g(C-C_\infty), \tag{2}$$

$$u\frac{\partial T}{\partial x}+\frac{\partial T}{\partial y}v+\Gamma^*\left(\begin{array}{l}\left(\frac{\partial}{\partial x}\left(\frac{\partial T}{\partial x}\right)\right)u^2+\left(\frac{\partial u}{\partial x}u+\frac{\partial u}{\partial y}v\right)\frac{\partial T}{\partial x}+v^2\left(\frac{\partial}{\partial y}\left(\frac{\partial T}{\partial y}\right)\right)\\+\frac{\partial T}{\partial y}\left(\frac{\partial v}{\partial y}v+\frac{\partial v}{\partial x}u\right)+2\left(\frac{\partial}{\partial x}\left(\frac{\partial T}{\partial y}\right)\right)uv\end{array}\right)$$

$$= \left( \frac{16\sigma * T_\infty^3}{3k *} \frac{\partial}{\partial y} \left( \frac{\partial}{\partial y} (T) \right) + \frac{\partial}{\partial y} \left( \frac{\partial}{\partial y} (T) \right) k_{hnf} \right) \frac{1}{(\rho C_p)_{hnf}} + \frac{1}{(\rho C_p)_{hnf}} \mu_{hnf} \left( \frac{\partial}{\partial y} (u) \frac{\partial}{\partial y} (u) \right) \tag{3}$$

$$u \frac{\partial}{\partial x} (C) + v \frac{\partial}{\partial y} (C) = D_m \frac{\partial}{\partial y} \left( \frac{\partial}{\partial y} (C) \right) - (C - C_\infty)^m k_1 \tag{4}$$

$$\left. \begin{array}{l} \text{at } y = 0: -k_{hnf} \left. \frac{\partial T}{\partial y} \right| = h_f (T_w - T), u = L_0 \frac{\partial}{\partial y} (u), v = 0, C = C_w, \\ \text{at } y \to \infty: C \to C_\infty, u \to U_\infty, T \to T_\infty . \end{array} \right\} \tag{5}$$

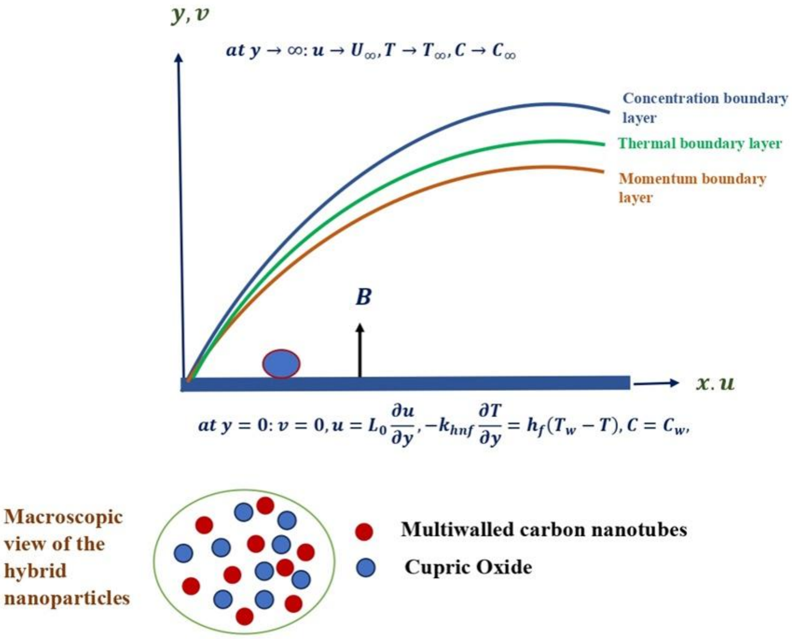


Fig. 1 Flow diagram

## 2.1 Hybrid nanofluid thermophysical features (Amala and Mahanthesh 2018)

$$\left. \begin{array}{l} (\rho C_p)_{hnf} = \left[ (1 - \phi_{MW})(\rho C_p)_f + \phi_M (\rho C_p)_{MW} \right] (1 - \phi_{Cu}) + (\rho C_p)_{Cu} \phi_{Cu}, \\ \sigma_{nf} = \sigma_f \times \dfrac{2\sigma_f + \sigma_{MW} - 2\phi_{MW}\sigma_f + 2\sigma_{MW}\phi_{MW}}{2\sigma_f + \sigma_{MW} + \phi_{MW}\sigma_f - \sigma_{MW}\phi_{MW}}, \\ \rho_{hnf} = [(1 - \phi_{MW})\rho_f + \phi_{MW}\rho_{MW}](1 - \phi_{Cu}) + \rho_{Cu}\phi_{Cu}, \\ \mu_{hnf} = \dfrac{\mu_f}{(1 - \phi_{MW})^{2.5}(1 - \phi_{Cu})^{2.5}}, \\ \sigma_{hnf} = \dfrac{2\sigma_{nf} + \sigma_{Cu} - 2\phi_{Cu}\sigma_{nf} + 2\sigma_{Cu}\phi_{Cu}}{2\sigma_{nf} + \sigma_{Cu} + \phi_{Cu}\sigma_{nf} - \sigma_{Cu}\phi_{Cu}} \times \sigma_{nf}. \end{array} \right\}$$

and

$$k_{hnf} = k_{nf} \times \frac{k_{Cu} + (l+1)k_{nf} - (l+1)k_{nf}\phi_{Cu} + (l+1)k_{Cu}\phi_{Cu}}{k_{Cu} + (l+1)k_{nf} + k_{nf}\phi_{Cu} - k_{Cu}\phi_{Cu}},$$

$$k_{nf} = k_f \times \frac{k_{MW} + (l+1)k_f - (l+1)k_f\phi_{MW} + (l+1)k_{MW}\phi_{MW}}{k_{MW} + (l+1)k_f + k_f\phi_{MW} - k_{MW}\phi_{MW}}.$$

(Sheikholeslami and Rokni 2017)

Where $l$ denotes the contour of the nanoparticle in this investigation. In this context, $l=1$ denotes a spherical form, $l=5.7$ signifies a platelet structure, and $l=4.8$ represents a cylindrical form.

Table 1. Thermo-physical parameters of water, CuO, and MWCNT utilized in the current study (source: Alzahrani et al., 2021).

| **Properties** | **MWCNT** ($\phi_{MW}$) | **$H_2O$** ($f$) | **CuO** ($\phi_{Cu}$) |
|---|---|---|---|
| $k(Wm^{-1}K^{-1})$ | 3000 | 0.613 | 76.5 |
| $\rho(kgm^{-3})$ | 2100 | 997.1 | 6320 |
| $\sigma(Sm^{-1})$ | 0.00019 | 0.0000055 | 2.7x10$^{-8}$ |
| $C_p(Jkg^{-1}K^{-1})$ | 711 | 4179 | 531.8 |

Using the similarity variables reported by Makinde (2013), the governing equations are reformulated into a dimensionless similarity framework for subsequent analysis.

$$\left.\Phi(\eta) = \frac{C-C_\infty}{C_w-C_\infty}, v = \sqrt{\frac{\upsilon U_\infty}{4x}}[\eta f'(\eta) - f(\eta)], \theta(\eta) = \frac{T-T_\infty}{T_w-T_\infty}, u = U_\infty f'(\eta), \eta = y\sqrt{\frac{U_\infty}{\upsilon x}}.\right\} \tag{6}$$

By substituting the similarity transformations given in Eq. (6) into Eq. (1), the continuity equation is satisfied identically. Terms in (6) can then be skillfully used to convert (2 - 5) as the following:

$$\frac{2}{S_1S_2}f''' + ff'' + 2\delta(\theta + \delta_1\Phi) - \frac{2}{S_1S_2}\frac{1}{\lambda}f' - 2Mg\frac{S_3}{S_1}(f' - 1) = 0, \tag{7}$$

$$\frac{S_4}{S_5} = \frac{2}{Pr\frac{2}{S_5}\frac{Ra}{Pr\frac{\Gamma^2}{2}\frac{\Gamma ff'\theta'}{2}\frac{2}{S_2S_5}^{2}}}, \tag{8}$$

$$\frac{2}{St}\Phi'' + f\Phi' - 2Cr\Phi^m = 0, \tag{9}$$

$$\left.\begin{aligned}&f(\eta)|_{\eta=0} = 0, f'(\eta)|_{\eta=0} = Lf''(\eta)|_{\eta=0}, \theta'(\eta)|_{\eta=0} = -\frac{Bi}{S_4}(1 - \theta(0)),\\&\Phi(\eta)|_{\eta=0} = 1, f'(\eta)|_{\eta\to\infty} = \frac{d}{d\eta}(f)\Big|_{\eta\to\infty} \to 1, \theta(\eta)|_{\eta\to\infty} \to 0, \Phi(\eta)|_{\eta\to\infty} \to 0,\end{aligned}\right\} \tag{10}$$

where

$$\left.\begin{aligned}&\delta = \frac{Gr}{Re_x^2}, Gr = \frac{g\beta_T(T_w - T_\infty)x^3}{\upsilon^2}, Re_x = \frac{xU_\infty}{\upsilon}, \delta_1 = \frac{Gc}{Gr}, Gc = \frac{g\beta_C(C_w - C_\infty)x^3}{\upsilon^2}, Bi = \frac{d}{k_f\sqrt{\frac{U_\infty}{\upsilon}}},\\&h_f = \frac{d}{\sqrt{x}}, Ra = \frac{16}{3}\frac{\sigma * T_\infty^3}{kk*}, St = \frac{\upsilon}{D_m}, \Gamma = \Gamma_0U_\infty, \Gamma^* = \Gamma_0x, Pr = \frac{\mu C_p}{k}, Cr = \frac{k_1(C_w - C_\infty)^{m-1}}{U_\infty},\\&k_0 = \frac{k_1}{x}, Mg = \frac{\sigma_fB_0^2}{\rho_fU_\infty}, B = \frac{B_0}{\sqrt{x}}, \lambda = \frac{\kappa_0U_\infty}{\upsilon}, \kappa_1 = \kappa_0x, Eck = \frac{U_\infty^2}{C_p(T_w - T_\infty)}, L = L_1\sqrt{\frac{U_\infty}{\upsilon}}, L_0 = L_1\sqrt{x},\end{aligned}\right\}$$

and

$$\left.\begin{aligned}&S_2 = (1 - \phi_{MW})^{2.5}(1 - \phi_{Cu})^{2.5}, S_5 = (1 - \phi_{Cu})\phi_{MW}\frac{(\rho C_p)_{MW}}{(\rho C_p)_f} + (1 - \phi_{Cu})(1 - \phi_{MW}) + \phi_{Cu}\frac{(\rho C_p)_{Cu}}{(\rho C_p)_f},\\&S_{31} = \frac{2\sigma_f + \sigma_{MW} - \phi_{MW}(2\sigma_f - 2\sigma_{MW})}{2\sigma_f + \sigma_{MW} + \phi_{MW}(\sigma_f - \sigma_{MW})}, S_1 = (1 - \phi_{Cu})\left[(1 - \phi_{MW}) + \phi_{MW}\frac{\rho_{MW}}{\rho_f}\right] + \phi_{Cu}\frac{\rho_{Cu}}{\rho_f},\\&S_3 = \frac{\sigma_{Cu} + 2S_{31}\sigma_f - 2\phi_{Cu}(S_{31}\sigma_f - \sigma_{Cu})}{\sigma_{Cu} + 2S_{31}\sigma_f + \phi_{Cu}(S_{31}\sigma_f - \sigma_{Cu})}S_{31}, S_4 = \frac{k_{Cu} + (l+1)S_{41}k_f - (l+1)(S_{41}k_f - k_{Cu})\phi_{Cu}}{k_{Cu} + (l+1)S_{41}k_f + (S_{41}k_f - k_{Cu})\phi_{Cu}}S_{41},\\&S_{41} = \frac{k_{MW} + (l+1)k_f - (l+1)(k_f - k_{MW})\phi_{MW}}{k_{MW} + (l+1)k_f + (k_f - k_{MW})\phi_{MW}}.\end{aligned}\right\}$$

The friction factor can be expressed using the subsequent formula:

$$Cf = \frac{1}{\rho}\frac{\partial u}{\partial y}\frac{\mu_{hnf}}{{U_\infty}^2}\bigg|_{y=0}. \tag{11}$$

Employing the similarity variables outlined in Eq. (6) enables the conversion of Eq. (11) into a compact dimensionless expression, thereby streamlining the mathematical formulation. $Cf = \frac{1}{\rho}\frac{\partial u}{\partial y}\frac{\mu_{hnf}}{{U_\infty}^2}\Big|_{y=0}$.

The subsequent relation is applied to determine the local Nusselt number for the heat transfer analysis.

$$Nu = -\frac{x}{k_f}\left(\frac{16}{3}\frac{T_\infty^3\sigma*}{k*} + k_{hnf}\right)\frac{1}{(T_w - T_\infty)}\frac{\partial T}{\partial y}\bigg|_{y=0}. \tag{12}$$

By employing (6), the formula presented in (12) can be succinctly reformulated as:

$$\sqrt{\frac{1}{Re_x}}Nu = -(S_4 + Ra)\theta'(0).$$

To figure out the mass transfer rate, one can utilize the following approach:

$$Sh = -x\frac{s_w}{D_m(C_w - C_\infty)}D_m\frac{\partial C}{\partial y}\bigg|_{y=0}. \tag{13}$$

By employing (6), the formulas utilized in (13) can be succinctly reformulated as:

$$\sqrt{\frac{1}{Re_x}}Sh = -\Phi'(0).$$

The dimensional expression for the entropy generation rate is given as follows.

$$S_g = \frac{1}{T_\infty^2}k_{hnf}\left(1 + \frac{16}{3}\frac{\sigma * T_\infty^3}{kk*}\right)\left(\frac{\partial}{\partial y}(T)\right)^2 + \mu_{hnf}\frac{1}{T_\infty}\left(\frac{\partial}{\partial y}(u)\right)^2 + \sigma_{hnf}\frac{1}{T_\infty}u^2B^2$$
$$+R_0D_m\frac{1}{T_\infty}\left(\frac{\partial C}{\partial y}\right)\left(\frac{\partial T}{\partial y}\right) + \frac{1}{C_\infty}R_0D_m\left(\frac{\partial}{\partial y}(C)\right)^2 \tag{14}$$

The incorporation of the transformations defined in Eq. (6) simplifies Eq. (14), yielding the following similarity equation. $N_{EG} = (S_4 + Ra)\beta\theta'^2 + \frac{1}{S_2}Brf''^2 + 2S_3MgBrf'^2 + H\Phi'\theta' + H\frac{\gamma}{\beta}\Phi'^2$ (15)

where

$$\left.\begin{array}{l} N_{EG} = \frac{x\upsilon S_g T_\infty}{U_\infty k_f(T_w - T_\infty)}, Br = \frac{\mu}{k_f}\frac{{U_\infty}^2}{(T_w - T_\infty)}, \beta = \frac{T_w - T_\infty}{T_\infty}, H = \frac{R_0 D_m(C_w - C_h)}{k_f}, \\ \gamma = \frac{C_w - C_\infty}{C_\infty}. \end{array}\right\}$$

To assess the balance between heat transfer and fluid friction irreversibility's, the Bejan number is determined through the analytical formulation given below.

$$Bn = \frac{\text{Irreversibility associated with heat and mass transport}}{\text{The whole entropy generation}}.$$

Applying (15) in the following way allows us to revise $Bn$:

$$Bn = \frac{(S_4 + Ra)\beta\theta'^2 + H\Phi'\theta' + H\frac{\gamma}{\beta}\Phi'^2}{(S_4 + Ra)\beta\theta'^2 + \frac{1}{S_2}Brf''^2 + 2S_3MgBrf'^2 + H\Phi'\theta' + H\frac{\gamma}{\beta}\Phi'^2}.$$

## 3. Computational Framework

The system of similarity equations (7)–(9), together with the relevant boundary conditions, is formulated as a boundary value problem. This problem is subsequently resolved numerically by employing the bvp4c algorithm within the MATLAB computational framework. For the numerical implementation, the bvp4c solver is adopted because of its capability to efficiently solve two-point boundary value problems through an adaptive collocation procedure utilizing the three-stage Lobatto IIIA formulation. An adaptive mesh refinement approach is employed to improve computational efficiency without compromising numerical accuracy. Owing to its stability, reliability, and accuracy, the bvp4c routine has proven to be a powerful computational approach for solving nonlinear boundary value problems encountered in fluid flow and heat transfer studies. A prerequisite for successful numerical convergence is a properly posed mathematical model together with an adequate set of boundary conditions that ensures the existence of a unique solution. Convergence difficulties may arise when the boundary value problem is ill posed or admits multiple solutions, which can prevent the numerical method from identifying a unique and physically meaningful solution.

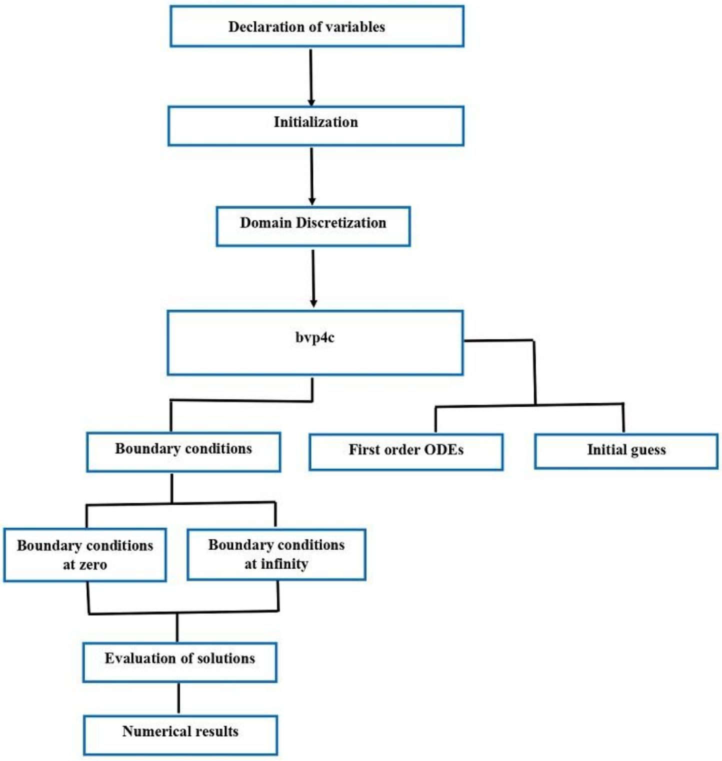


Figure 2: Flow diagram of BVP4C numerical scheme. (adapted from Faiz et al., 2022).

## 4. Verification of the current outcomes

The findings of our work have been corroborated through comparison with former reported findings, specifically within specific settings. A good agreement is noticed (refer to Table-2).

Table 2: To ensure reliability, the computational results obtained in this study are benchmarked against existing literature, focusing on representative limiting conditions for meaningful validation. *Pr=10* and $\phi_{MW}=\phi_{Cu}=0$.

| $Bi$ | $-\theta'(0)$ | |
|---|---|---|
| | Daniel (2016) | Present results |
| 1 | 0.42130 | 0.421344 |
| 5 | 0.63551 | 0.635583 |
| 10 | 0.67853 | 0.678721 |
| 20 | 0.70256 | 0.702563 |

## 5. Discussion of outcomes

The three cases involving the shape factor—platelet, cylinder, and spherical—are addressed with the results.

## 5.1 Regular profiles including temperature

The velocity of the fluid decreases progressively with higher values of the MWCNT volume fraction ($\phi_{MW}$), since the enhanced effective viscosity imposes additional resistance to flow. This trend is clearly demonstrated in Fig. 3. At higher volume fractions, nanoparticles begin to interact with each other more frequently. Enhanced interactions among nanoparticles may facilitate agglomeration, causing an uneven particle distribution that introduces localized flow disturbances and lowers the overall heat transfer efficiency. An external magnetic field introduces Lorentz forces that counteract fluid motion, reducing velocity as field strength rises (Fig. 4). This trend is consistent with MHD principles. In parallel, higher thermal radiation parameters intensify radiative heat transfer, increasing energy absorption and emission within the fluid. The resulting effect elevates fluid temperature and alters its distribution, particularly under larger temperature gradients (Fig. 5). As the Eckert number grows, viscous dissipation becomes more pronounced, channelling kinetic energy into thermal energy and thereby elevating the fluid temperature, as shown in Fig. 6. A higher MWCNT volume fraction ($\phi_{MW}$) further augments the nanofluid's thermal conductivity, intensifying heat transfer and producing a more elevated temperature distribution, as seen in Fig. 7. With increasing nanoparticle concentration, the hybrid nanofluid exhibits enhanced thermal conductivity, which facilitates efficient heat diffusion and leads to greater thermal energy accumulation. At the same time, the rise in nanoparticle content increases viscosity, making viscous friction more significant. This frictional mechanism converts part of the flow's mechanical energy into internal energy, contributing to a small but noticeable increase in fluid temperature. The notion of thermal relaxation time captures the delay involved in transmitting heat from a fluid particle to the adjacent medium. Higher relaxation times weaken the rate of energy exchange, thereby slowing thermal diffusion and extending heat retention within the fluid. As thermal energy transfer slows, the fluid temperature declines, as shown in Fig. 8. When the chemical reaction parameter is increased, the reaction becomes more intense, leading to faster consumption of reactive species. This process reduces species concentration, compresses the boundary layer, and lowers the concentration profile, as demonstrated in Fig. 9. The influence of the Schmidt number ($S_t$) is evident in Fig. 10, where higher values correspond to reduced species diffusion. In such cases, momentum diffusivity outweighs mass diffusivity, thereby diminishing concentration levels throughout the boundary layer.

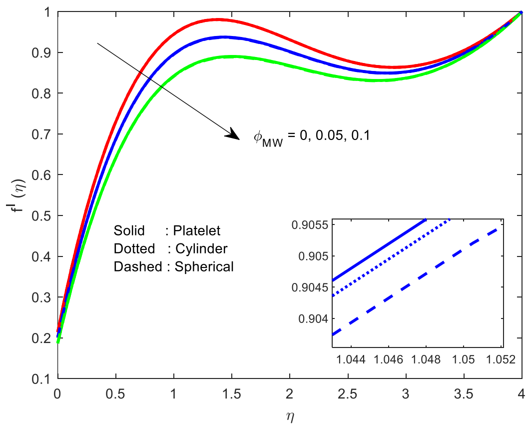


Fig. 3: Effect of MWCNT concentration ($\phi_{MW}$) on velocity distribution of the fluid

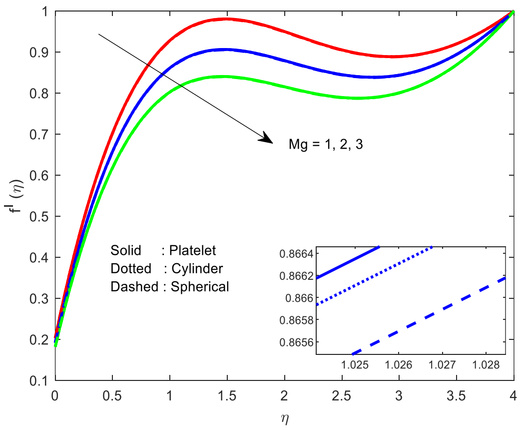


Fig. 4: Velocity distribution for varying magnitudes of the magnetic parameter ($M_g$).

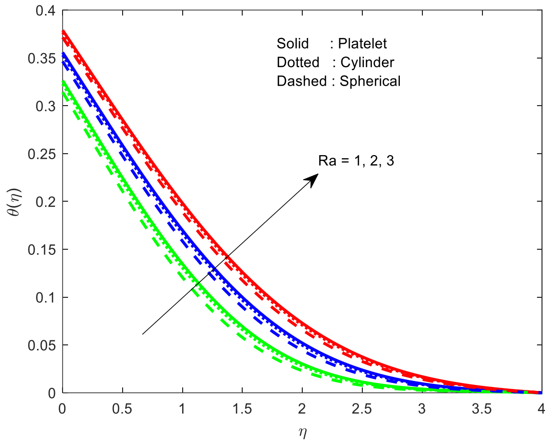


Fig. 5 Impact of *Ra* on temperature profile

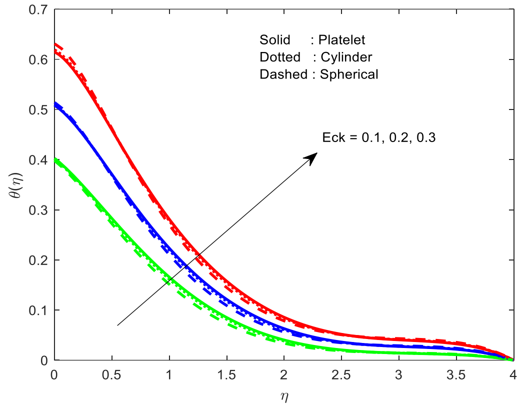


Fig. 6 Impact of *Eck* on temperature profile

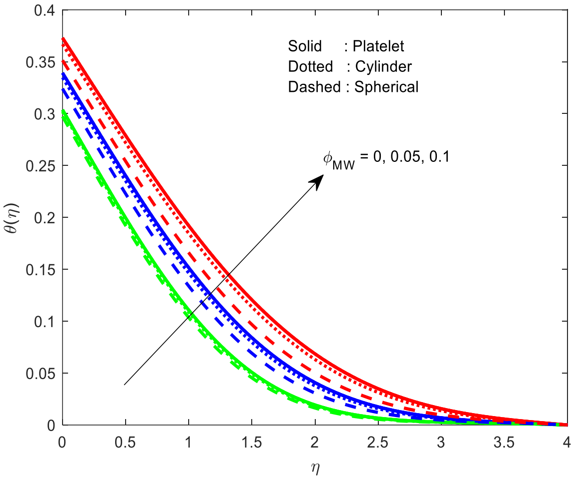


Fig. 7: Variation of temperature distribution with MWCNT volume fraction.

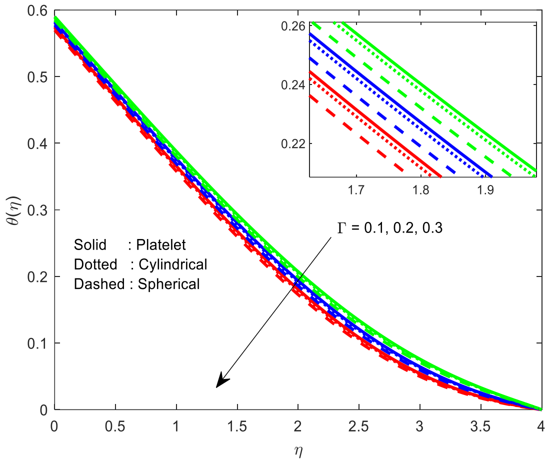


Fig. 8: Illustration of how changes in the parameter Γ influence the fluid's temperature distribution.

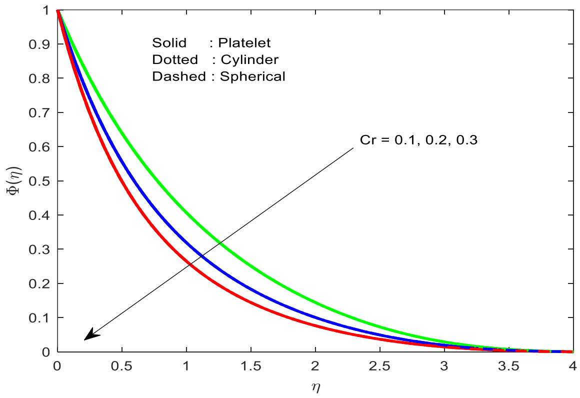


Fig. 9: Variation of concentration distribution with the chemical reaction parameter (Cr).

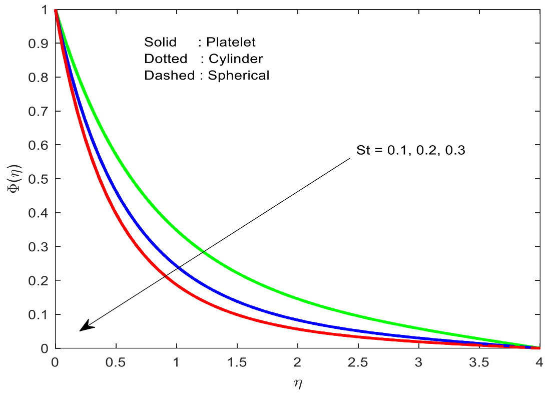


Fig. 10: Impact of St on concentration profile

## 5.2 Analysis of Bejan number trends and entropy generation distributions

Fig. 11. Rising Brinkman number amplifies viscous dissipation, leading to greater entropy generation and irreversibility. The augmented viscous dissipation results in enhanced energy dissipation and, therefore, an elevated rate of entropy formation. The creation of entropy in a fluid flow is directly proportional to both the volume fractions of MWCNT and *CuO*, as shown in Figs. 12-13. With greater nanoparticle loading, the nanofluid's effective viscosity rises, leading to stronger viscous friction and higher energy dissipation. This process amplifies entropy generation through intensified irreversibility. Figs. 14–15 illustrate that the Bejan number serves as a measure of the relative contributions of thermal and frictional mechanisms to entropy production. Although the MWCNT volume fraction ($\phi_{MW}$) influences this parameter indirectly, an increase in the Brinkman number shifts the balance, resulting in a decline in the Bejan number. Higher Brinkman numbers enhance the contribution of viscous dissipation to thermodynamic irreversibility, thereby increasing entropy generation associated with fluid friction. As a consequence, the contribution of frictional irreversibility becomes more significant than thermal irreversibility. Since the Bejan number represents the relative role of heat transfer irreversibility in overall entropy production, its value diminishes when the Brinkman number increases, as viscous dissipation exerts a greater influence on thermodynamic irreversibility. Larger Brinkman numbers therefore highlight the predominance of frictional losses over thermal effects. This trend is further evident in Fig. 16, where the Bejan number decreases with rising MWCNT volume fraction ($\phi_{MW}$).

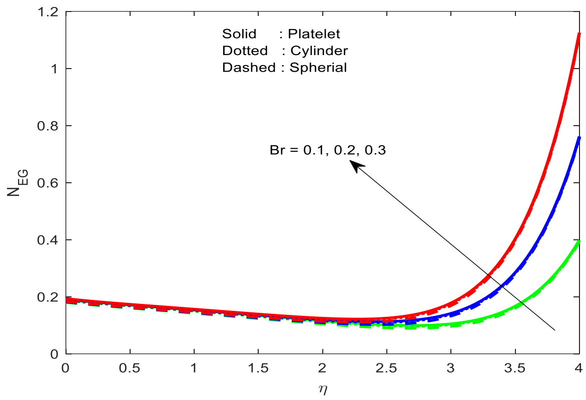


Fig. 11 Impact of Br on $N_{EG}$

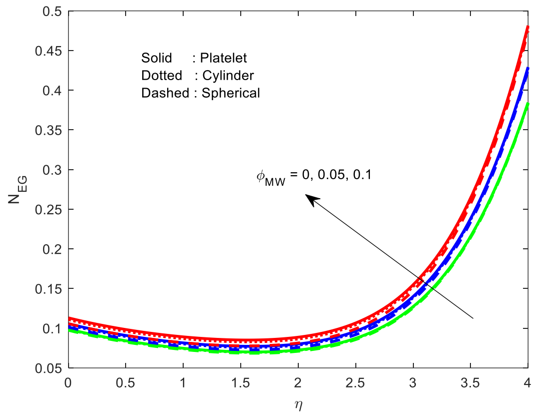


Fig. 12 Impact of $\phi_{MW}$ on $N_{EG}$

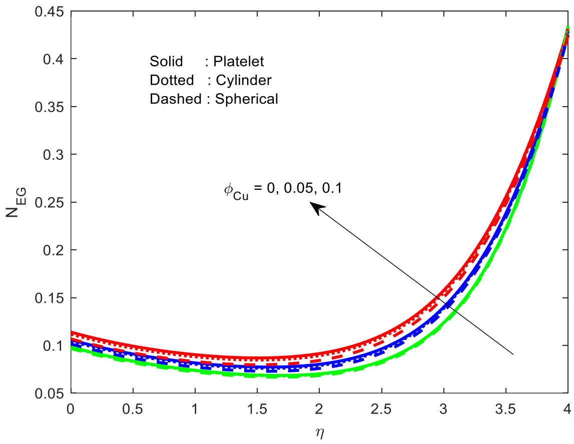


Fig. 13: $N_{EG}$ distribution corresponding to different values of ($\phi_{Cu}$).

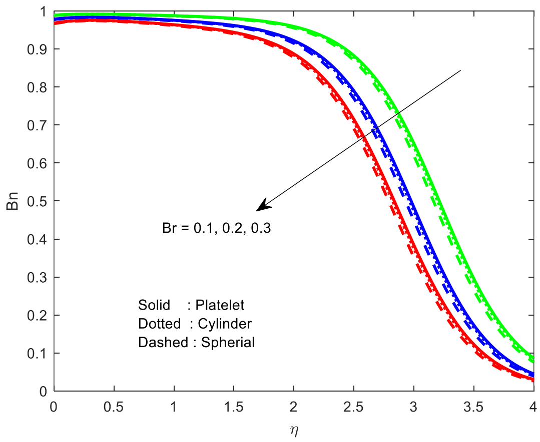


Fig. 14: Impact of Br on Bn

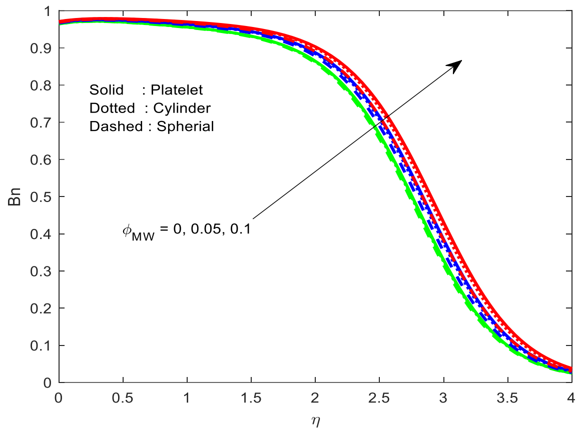


Fig. 15 Impact of $\phi_{MW}$ on Bn

## 5.3 Engineering quantities including Nusselt number

As presented in Table 3, the applied magnetic field ($M_g$) together with nanoparticle interactions significantly modify the flow, thereby impacting the skin-friction coefficient. The increase in $\phi_{MW}$ enhances the effective viscosity of the hybrid nanofluid, which strengthens interparticle interactions and raises momentum resistance. This adjustment in rheological behavior intensifies shear forces at the wall, ultimately producing a higher skin-friction coefficient. The friction factor is also marginally influenced by nanoparticle morphology; as different particle geometries produce distinct flow responses under identical conditions. The observed modifications in the Nusselt number under varying Γ and Eckert numbers highlight the competing influences of convective and conductive mechanisms. The finite nature of the thermal response is determined by the relaxation parameter, coupled with the inherent thermophysical properties of the medium. The finite thermal response associated with larger values of (Γ) delays energy exchange between the fluid and its surroundings, thereby diminishing convective heat transfer. s reported in Table 4, the Nusselt number decreases due to the combined effects of convection and conduction. In contrast, the Eckert number reflects the contribution of viscous dissipation to heat generation relative to the fluid's conductive capacity. Table 5 reveals that both the chemical reaction parameter ($C_r$)) and the Schmidt number (St) enhance mass transfer, leading to an increase in the Sherwood number. The higher chemical reaction intensity enhances species depletion near the surface, resulting in a steeper concentration gradient and improved mass transfer characteristics. The Sherwood number exhibits a positive response to increasing chemical reaction strength. When $C_r$ varies between 0 and 0.6, the enhancement in the Sherwood number is found to be 0.2827136, 0.2827211, and 0.2827408 for platelet, cylindrical, and spherical nanoparticle shapes, respectively.

Table 3. Variation in skin-friction coefficient as influenced by changes in the magnetic parameter and MWCNT volume fraction.

| $Mg$ | $\phi_{MW}$ | Platelet | Cylinder | Spherical |
|---|---|---|---|---|
| 1 | | 0.065866 | 0.065843 | 0.065781 |
| 2 | | 0.0262 | 0.026195 | 0.026182 |
| 3 | | 0.015076 | 0.015076 | 0.015073 |
| 4 | | 0.010683 | 0.010684 | 0.010684 |
| | 0 | 0.015516 | 0.015515 | 0.015513 |
| | 0.045 | 0.016382 | 0.016381 | 0.016378 |
| | 0.075 | 0.017126 | 0.017124 | 0.017121 |
| | 0.105 | 0.018027 | 0.018026 | 0.018022 |

Table 4 Impact of $\Gamma$ and $Eck$ on Nusselt number

| $\Gamma$ | $Eck$ | Platelet | Cylinder | Spherical |
|---|---|---|---|---|
| 0 | | 0.246657 | 0.239636 | 0.222954 |

| | | | | |
|---|---|---|---|---|
| 0.1 | | 0.245578 | 0.238553 | 0.221859 |
| 0.2 | | 0.2444432 | 0.237411 | 0.220702 |
| 0.3 | | 0.243249 | 0.236208 | 0.219474 |
| | 0 | 0.792512 | 0.765672 | 0.703459 |
| | 0.2 | 0.703276 | 0.676414 | 0.614177 |
| | 0.4 | 0.614387 | 0.587496 | 0.525327 |
| | 0.6 | 0.525839 | 0.498971 | 0.436809 |

**Table 5** Impact of $Cr$ and $St$ on Sherwood number

| $Cr$ | $St$ | Platelet | Cylinder | Spherical |
|---|---|---|---|---|
| 0 | | 0.260261 | 0.260249 | 0.260215 |
| 0.2 | | 0.322948 | 0.322937 | 0.322909 |
| 0.4 | | 0.379120 | 0.379110 | 0.379086 |
| 0.6 | | 0.430263 | 0.430255 | 0.430233 |
| | 0 | 0.25 | 0.25 | 0.25 |
| | 0.2 | 0.320092 | 0.320084 | 0.320065 |
| | 0.4 | 0.381570 | 0.381558 | 0.381526 |
| | 0.6 | 0.436702 | 0.436686 | 0.436643 |

## 6. Conclusions

This study investigates the intricate dynamics of hybrid nanofluid ($H_2O+MWCNT+C_uO$) flow via a flat plate, analyzing the influence of several physical parameters including velocity slip, form factor, and thermal radiation. The three cases involving the shape factor—platelet, cylinder, and spherical—are addressed with the results. Key findings are presented below:

- As Br and $\phi_{MW}$ values rise, the entropy generation also rises.
- Increasing the MWCNT loading enhances the frictional resistance of the nanofluid. As $\phi_{MW}$ changes from 0 to 0.105, the friction factor increments are obtained as 0.02383, 0.023825, and 0.023809 for platelet, cylindrical, and spherical particle shapes, respectively.
- Research indicates that when the Eckert number varies from 0 to 0.6, the heat transmission rate decreases by 0.4444371 for platelet form, 0.444998 for cylindrical form, and 0.444502 for spherical form.
- An intensified magnetic field strengthens the Lorentz force, which opposes fluid motion. This added electromagnetic resistance diminishes fluid momentum, thereby lowering the velocity profile.
- An intensified thermal radiation effect strengthens the coupling between radiative energy and the fluid, thereby increasing heat absorption and elevating the fluid temperature.
- Longer relaxation time delays heat transport, diminishing energy exchange and lowering temperature.
- As the chemical reaction parameter varies from 0 to 0.6, the Sherwood number demonstrates a notable rise. The enhancement rates are 0.2827136 for platelet structures, 0.2827211 for cylindrical forms, and 0.2827408 for spherical particles, highlighting the influence of nanoparticle geometry on mass transfer behavior.

### CRediT Author Statement

**Dr. Kathyayani:** Supervision, Validation, Editing and Rewriting.
**Satya Nagendra Rao:** Conceptualization, Methodology, Software, Writing- Original draft preparation, Validation.

## Acknowledgements

The authors received no financial support for the research, authorship, and publication of this article.

## References

Acharya, N., Maity, S., and Kundu, P. K. (2020). Framing the hydrothermal features of magnetized $TiO_2$–$CoFe_2O_4$ water-based steady hybrid nanofluid flow over a radiative revolving disk. Multidiscipline Modeling in Materials and Structures, 16(4), 765–790. https://doi.org/10.1108/MMMS-08-2019-0151

Afridi, M. I., Qasim, M., and Saleem, S. (2018). Second law analysis of three-dimensional dissipative flow of hybrid nanofluid. Journal of Nanofluids, 7(6), 1272–1280. https://doi.org/10.1166/jon.2018.1532

Al-Harbi, S. M. (2005). Numerical study of natural convection heat transfer with variable viscosity and thermal radiation from a cone and wedge in porous media. Applied Mathematics and Computation, 170(1), 64–75. https://doi.org/10.1016/j.amc.2004.10.093

Al-Hossainy, A. F., and Eid, M. R. (2021). Combined experimental thin films, TDDFT-DFT theoretical method, and spin effect on PEG–$H_2O$/$ZrO_2$ + MgO hybrid nanofluid flow with higher chemical rate. Surfaces and Interfaces, 23, 100971. https://doi.org/10.1016/j.surfin.2021.100971

Ali Ghazwani, H. (2024). Time-dependent mixed stagnation point hybrid nanofluid flow with radiative heat flux and viscous dissipation effects over a movable EMHD Riga plate. International Journal of Modern Physics B, 38(6), 2450090. https://doi.org/10.1142/S0217979224500905

Alzahrani, A. K., Ullah, M. Z., Alshomrani, A. S., and Gul, T. (2021). Hybrid nanofluid flow in a Darcy–Forchheimer permeable medium over a flat plate due to solar radiation. Case Studies in Thermal Engineering, 26, 100955. https://doi.org/10.1016/j.csite.2021.100955

Amala, S., and Mahanthesh, B. (2018). Hybrid nanofluid flow over a vertical rotating plate in the presence of Hall current, nonlinear convection and heat absorption. Journal of Nanofluids, 7(6), 1138–1148. https://doi.org/10.1166/jon.2018.1550

Anantha Kumar, K., Sugunamma, V., and Sandeep, N. (2020). Effect of thermal radiation on MHD Casson fluid flow over an exponentially stretching curved sheet. Journal of Thermal Analysis and Calorimetry, 140, 2377–2385. https://doi.org/10.1007/s10973-019-08977-0

Animasaun, I. L., Al-Mdallal, Q. M., Khan, U., and Alshomrani, A. S. (2022). Unsteady water-based ternary hybrid nanofluids on wedges by bioconvection and wall stretching velocity: Thermal analysis and scrutinization of small and larger magnitudes of the thermal conductivity of nanoparticles. Mathematics, 10(22), 4309. https://doi.org/10.3390/math10224309

Appidi, L., Malga, B. S., and Pramod Kumar, P. (2022). Effect of thermal radiation on an unsteady MHD flow over an impulse vertical infinite plate with variant temperature in existence of Hall current. Heat Transfer, 51(3), 2367–2382. https://doi.org/10.1002/htj.22402

Babu, M. J., Rao, Y. S., Kumar, A. S., Raju, C. S. K., Shehzad, S. A., Ambreen, T., and Shah, N. A. (2022). Squeezed flow of polyethylene glycol and water based hybrid nanofluid over a magnetized sensor surface: A statistical approach. International Communications in Heat and Mass Transfer, 135, 106136. https://doi.org/10.1016/j.icheatmasstransfer.2022.106136

Bakier, A. Y., and Reddy Gorla, R. S. (1996). Thermal radiation effect on mixed convection from horizontal surfaces in saturated porous media. Transport in Porous Media, 23, 357–363. https://doi.org/10.1007/BF00167104

Bidin, B., and Nazar, R. (2009). Numerical solution of the boundary layer flow over an exponentially stretching sheet with thermal radiation. European Journal of Scientific Research, 33(4), 710–717.

Cao, W., Animasaun, I. L., Yook, S. J., Oladipupo, V. A., and Ji, X. (2022). Simulation of the dynamics of colloidal mixture of water with various nanoparticles at different levels of partial slip: Ternary hybrid nanofluid. International Communications in Heat and Mass Transfer, 135, 106069. https://doi.org/10.1016/j.icheatmasstransfer.2022.106069

Daniel, Y. S. (2016). Laminar convective boundary layer slip flow over a flat plate using homotopy analysis method. Journal of the Institution of Engineers (India): Series E, 97, 115–121. https://doi.org/10.1007/s40034-016-0084-6

Faiz, M., Habib, D., Siddique, I., Awrejcewicz, J., Pawłowski, W., Abdal, S., and Salamat, N. (2022). Multiple slip effects on time dependent axisymmetric flow of magnetized Carreau nanofluid and motile microorganisms. Scientific Reports, 12(1), 14259. https://doi.org/10.1038/s41598-022-18344-z

Gohar, Taza, G., Waris, K., Muhammad, S., Muhammad, A. K., and Ebenezer, B. (2019). MWCNTs/SWCNTs nanofluid thin film flow over a nonlinear extending disc: OHAM solution. Journal of Thermal Science, 28, 115–122. https://doi.org/10.1007/s11630-018-1075-3

Hassan, A. R., and Fenuga, O. J. (2019). The effects of thermal radiation on the flow of a reactive hydromagnetic heat generating couple stress fluid through a porous channel. SN Applied Sciences, 1(10), 1278. https://doi.org/10.1007/s42452-019-1300-z

Hussain, S., Ahmed, S. E., and Akbar, T. (2017). Entropy generation analysis in MHD mixed convection of hybrid nanofluid in an open cavity with a horizontal channel containing an adiabatic obstacle. International Journal of Heat and Mass Transfer, 114, 1054–1066. https://doi.org/10.1016/j.ijheatmasstransfer.2017.06.135

Kathyayani, G. (2021). MHD mixed convection Jeffrey fluid near a stagnation-point flow of induced magnetic field and linear/non-linear vertical stretching sheet with chemical reaction in the presence of thermal radiation and suction or injection. Turkish Journal of Computer and Mathematics Education, 12(13), 2453–2464.

Koo, J., and Kleinstreuer, C. (2005). Laminar nanofluid flow in microheat-sinks. International Journal of Heat and Mass Transfer, 48(13), 2652–2661. https://doi.org/10.1016/j.ijheatmasstransfer.2005.01.029

Lund, L. A., Omar, Z., Khan, I., Baleanu, D., and Nisar, K. S. (2020). Dual similarity solutions of MHD stagnation point flow of Casson fluid with effect of thermal radiation and viscous dissipation: Stability analysis. Scientific Reports, 10(1), 15405. https://doi.org/10.1038/s41598-020-72266-2

Majeed, A., Zeeshan, A., and Alam, T. (2023). Mathematical analysis of MHD CNTs of rotating nanofluid flow over a permeable stretching surface. Arabian Journal for Science and Engineering, 48(1), 727–737. https://doi.org/10.1007/s13369-022-06871-w

Makhdoum, B. M., Mahmood, Z., Fadhl, B. M., Aldhabani, M. S., Khan, U., and Eldin, S. M. (2023). Significance of entropy generation and nanoparticle aggregation on stagnation point flow of nanofluid over stretching sheet with inclined Lorentz force. Arabian Journal of Chemistry, 16(6), 104787. https://doi.org/10.1016/j.arabjc.2023.104787

Makinde, O. D., Gnaneswara Reddy, M., and Venugopal Reddy, K. (2017). Effects of thermal radiation on MHD peristaltic motion of Walters-B fluid with heat source and slip conditions. Journal of Applied Fluid Mechanics, 10(4), 1105–1112. https://doi.org/10.18869/acadpub.jafm.73.241.27082

Makinde, O. D. (2013). Effects of viscous dissipation and Newtonian heating on boundary-layer flow of nanofluids over a flat plate. International Journal of Numerical Methods for Heat and Fluid Flow, 23(8), 1291–1303. https://doi.org/10.1108/HFF-12-2011-0258

Moghaddami, M., Mohammadzade, A., and Esfehani, S. A. V. (2011). Second law analysis of nanofluid flow. Energy Conversion and Management, 52(2), 1397–1405. https://doi.org/10.1016/j.enconman.2010.10.002

Mohammadein, A. A., and El-Amin, M. F. (2000). Thermal radiation effects on power-law fluids over a horizontal plate embedded in a porous medium. International Communications in Heat and Mass Transfer, 27(7), 1025–1035. https://doi.org/10.1016/S0735-1933(00)00182-2

Nadeem, S., Ishtiaq, B., and Abbas, N. (2023). Impact of thermal radiation on two-dimensional unsteady third-grade fluid flow over a permeable stretching Riga plate. International Journal of Modern Physics B, 37(1), 2350009. https://doi.org/10.1142/S0217979223500091

Purna Chandar Rao, D., Thiagarajan, S., and Srinivasa Kumar, V. (2022). Significance of quadratic thermal radiation on the bioconvective flow of Ree–Eyring fluid through an inclined plate with viscous dissipation and chemical reaction: Non-Fourier heat flux model. International Journal of Ambient Energy, 43(1), 6436–6448. https://doi.org/10.1080/01430750.2021.2023043

Qasem, S. A., Sivasankaran, S., Siri, Z., and Othman, W. A. (2021). Effect of thermal radiation on natural convection of a nanofluid in a square cavity with a solid body. Thermal Science, 25(3), 1949–1961. https://doi.org/10.2298/TSCI191003182Q

Reddy, M. G., Kumari, P. V., and Padma, P. (2018). Effect of thermal radiation on MHD Casson nanofluid over a cylinder. Journal of Nanofluids, 7(3), 428–438. https://doi.org/10.1166/jon.2018.1467

Revathi, G., Reddy, S. N., Babu, M. J., and Mahesh, B. (2024). Impact of activation energy and thermal radiation on hybrid nanofluid (engine oil + nickel zinc ferrite + manganese zinc ferrite) flow over a wavy cylinder in the presence of induced magnetic field. Proceedings of the Institution of Mechanical Engineers, Part E: Journal of Process Mechanical Engineering. Advance online publication. https://doi.org/10.1177/09544089241274988

Revathi, G., Sajja, V. S., Raju, C. S. K., and Babu, M. J. (2021). Numerical simulation for Arrhenius activation energy on the nanofluid dissipative flow by a curved stretching sheet. The European Physical Journal Special Topics, 230(5), 1283–1292. https://doi.org/10.1140/epjs/s11734-021-00048-6

Roy, N. C., Hossain, M. A., and Pop, I. (2021). Analysis of dual solutions of unsteady micropolar hybrid nanofluid flow over a stretching/shrinking sheet. Journal of Applied and Computational Mechanics, 7(1), 19–33. https://doi.org/10.22055/jacm.2020.34686.2457

Sandeep, N., Ranjana, B., Samrat, S. P., and Ashwinkumar, G. P. (2022). Impact of nonlinear radiation on magnetohydrodynamic flow of hybrid nanofluid with heat source effect. Proceedings of the Institution of Mechanical Engineers, Part E: Journal of Process Mechanical Engineering, 236(4), 1616–1627. https://doi.org/10.1177/09544089211070667

Shaheen, A., Waqas, H., Imran, M., Raza, M., and Rashid, S. (2024). The effects of thermal radiation and heat source/sink on the flow and heat transfer characteristics of a hybrid nanofluid over a vertical stretching cylinder: Regression analysis. International Journal of Modern Physics B, 38(29), 2450397. https://doi.org/10.1142/S0217979224503971

Sheikholeslami, M., and Rokni, H. B. (2017). Magnetic nanofluid natural convection in the presence of thermal radiation considering variable viscosity. The European Physical Journal Plus, 132, 1–12. https://doi.org/10.1140/epjp/i2017-11498-4

Thameem Basha, H., Sivaraj, R., Subramanyam Reddy, A., and Chamkha, A. J. (2019). SWCNH/diamond–ethylene glycol nanofluid flow over a wedge, plate and stagnation point with induced magnetic field and nonlinear radiation: Solar energy application. The European Physical Journal Special Topics, 228, 2531–2551. https://doi.org/10.1140/epjst/e2019-900048-x

Ullah, I., Shukat, S., Albakri, A., Khan, H., Galal, A. M., and Jamshed, W. (2023). Thermal performance of aqueous alumina–titania hybrid nanomaterials dispersed in rotating channel. International Journal of Modern Physics B, 37(24), 2350237. https://doi.org/10.1142/S0217979223502375

Upreti, H., and Kumar, M. (2020). Influence of non-linear radiation, Joule heating and viscous dissipation on the boundary layer flow of MHD nanofluid flow over a thin moving needle. Multidiscipline Modeling in Materials and Structures, 16(1), 208–224. https://doi.org/10.1108/MMMS-05-2019-0097

Waqas, M., Khan, U., Zaib, A., Ishak, A., Albaqami, M. D., Waini, I., Alotabi, R. G., and Pop, I. (2023). Radiation effect on MHD three-dimensional stagnation-point flow comprising water-based graphene oxide nanofluid induced by a nonuniform heat source/sink over a horizontal plane surface. International Journal of Modern Physics B, 37(15), 2350146. https://doi.org/10.1142/S0217979223501461

Xiu, W., Animasaun, I. L., Al-Mdallal, Q. M., Alzahrani, A. K., and Muhammad, T. (2022). Dynamics of ternary-hybrid nanofluids due to dual stretching on wedge surfaces when volume of nanoparticles is small and large: Forced convection of water at different temperatures. International Communications in Heat and Mass Transfer, 137, 106241. https://doi.org/10.1016/j.icheatmasstransfer.2022.106241